

Nematic Order in Twisted Bilayer Graphene by Valley + Spin Fluctuation Interference Mechanism

Seiichiro Onari and Hiroshi Kontani

Department of Physics, Nagoya University, Furo-cho, Nagoya 464-8602, Japan.

(Dated: January 26, 2022)

In the magic angle twisted bilayer graphene (TBG), one of the most remarkable observations is the C_3 -symmetry-breaking nematic state. We identify that the nematicity in TBG is the E -symmetry ferro bond order, which is the symmetry breaking in the effective hopping integrals. Thanks to the strong correlation and valley degree of freedom characteristics of the TBG, the nematicity in the TBG originates from prominent quantum interference among valley fluctuations and spin fluctuations. This novel “valley + spin fluctuation interference mechanism” also causes novel time-reversal-symmetry-broken valley polarization accompanied by a charge loop current. We discuss interesting similarities and differences between the TBG and Fe-based superconductors.

The emergence of the exotic electronic states in the magic angle ($\sim 1.1^\circ$) twisted bilayer graphene (TBG) opens a novel platform of strongly correlated electron systems [1–4]. Since the moiré pattern in the TBG makes superlattice, nearly flat band due to the multi band folding appears around the charge neutrality. The nearly flat band provides the strong correlation system with many van Hove singularity (VHS) points. The superconducting phase broadly appears near the VHS filling $n \sim \pm 2$, where n denotes number of electrons in the moiré superlattice unit cell, and $n = 0$ corresponds to the charge neutrality. A lot of important theoretical studies have been performed in the last few years [5–18].

Recently, the ferro ($\mathbf{q} = \mathbf{0}$) C_3 -symmetry-breaking nematic state has been observed by STM and resistivity anisotropy measurements in the TBG [19–22]. In the vicinity of the VHS filling, the electronic nematic state appears in the metallic phase [19, 22]. To explain the nematicity in the TBG, the acoustic phonon mechanism has been proposed [23] by restricting to the ferro order ($\mathbf{q} = \mathbf{0}$). Also, the electron correlation mechanism has been studied using the renormalization group (RG) theory [24]. However, the following fundamental questions remain open problems: What is the driving force of the nematicity? Why the nematic order is selected over rich degrees of freedom in the TBG? Also, why the nematic order is $\mathbf{q} = \mathbf{0}$?

The nematic orders are also realized in Fe-based and cuprate superconductors [25–27]. Both the spin-nematic [28–34] and orbital/bond-order [35–47] scenarios have been applied to solve this issue. It was revealed that the nematic orbital/bond orders are generated by the paramagnon interference shown in Fig. 1(a) [39–42, 47]. Its significance has been confirmed by the functional RG studies [45–48]. This mechanism may also be applicable to TBG. On the other hand, the TBG has two significant characteristics distinct from usual transition metal compounds; (i) presence of the valley degree of freedom ξ , and (ii) absence of on-site Hund’s coupling $J = 0$ [49, 50]. By focusing on both (i) and (ii), we explain why rich unconventional density waves appear in TBG.

In this paper, we study the origin of the nematic state in the TBG by focusing on the two significant features, (i) the presence of the valley and (ii) the absence of J . We predict that the $\mathbf{q} = \mathbf{0}$ nematic bond order naturally emerges near the VHS filling n_{VHS} , consistently with experiments [19–22]. The nematic bond order is driven by the interferences among the valley + spin fluctuations thanks to the Hund’s less nature of the TBG. This interference mechanism also causes the time-reversal-symmetry-broken valley polarization accompanied by a novel charge loop current. This study reveals interesting similarities and differences between the TBG and Fe-based superconductors.

As for the character (i), the Wannier orbitals 1 and 2 (3 and 4) in Fig. 1(b) are labeled as the valley $\xi = +1$ (-1). The FSs are also labeled by the valley ξ since inter-valley hopping integrals are absent. The valley ξ changes its sign under the time reversal operation. As for the character (ii), the intra- and inter-valley on-site Coulomb repulsions are exactly the same ($U = U'$), and the Hund’s coupling is zero [49, 50]. Both (i) and (ii) are key ingredients in the rich unconventional density waves obtained in the present study.

We analyze the following two-dimensional four-orbital Hubbard model [40]:

$$H = H^0 + H^U, \quad (1)$$

where H^0 is the first-principles model for the TBG in Ref. [49] with minimum additional terms to make $n_{\text{VHS}} \sim 2$, as we explain in Supplementary Material (SM) A [51]. Figure 1(b) shows Moiré superlattice spanned by the AA spots. We define the distance between the nearest AA spots as 1. At the AB (BA) spots, the A (B) sublattice in upper graphene layer just locates above B (A) sublattice in lower one. The centers of Wannier orbitals 1, 3 and 2, 4 locate at the BA and AB spots, respectively. The orbitals 1 and 2 ($\xi = +1$) are transformed to the orbitals 3 and 4 ($\xi = -1$) by the time-reversal operation, respectively. Each valley is independent in H^0 : $H^0 = H_{\xi=+1}^0 + H_{\xi=-1}^0$. H^U is the Coulomb interaction. We consider the intra-valley local Coulomb interaction U and inter-valley one

U' on the same AB, BA sites. The relations $U' = U$ and $J = 0$ are satisfied in the Wannier orbitals of the TBG [49, 50]. Details of model and interaction are presented in SM A [51].

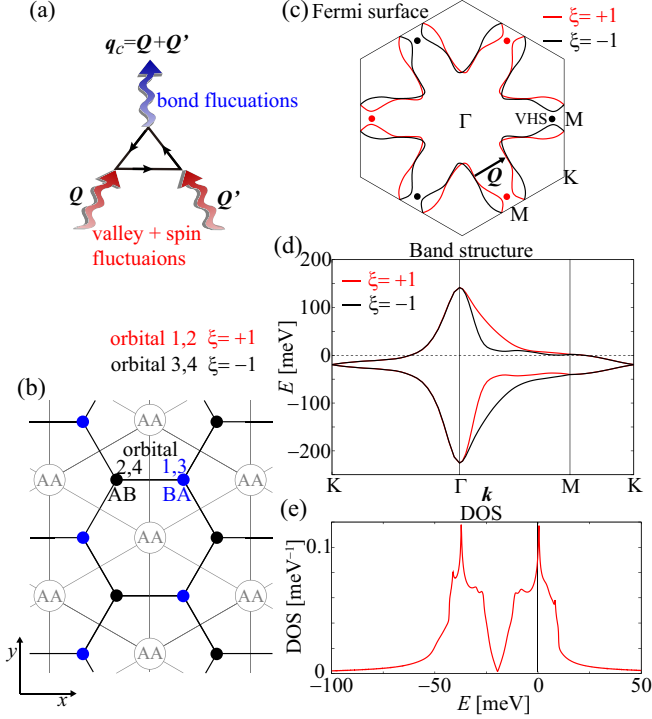


FIG. 1. (a) Quantum interference between valley+spin fluctuations with the wavevector \mathbf{Q} and \mathbf{Q}' , which induces the bond fluctuations with $\mathbf{q}_c = \mathbf{Q} + \mathbf{Q}'$. (b) Moiré superlattice spanned by the AA spots. Wannier orbitals 1, 3 and 2, 4 are centered at the BA (blue dots) and AB (black dots) spots, respectively. (c) FSs of the TBG for $n = 2.0$, where red (black) lines and dots denote the valley and the VHS points for $\xi = +1$ (-1), respectively. The vector \mathbf{Q} is the nesting vector. (d) Band structure and (e) DOS of the TBG model for $n = 2.0$.

Here, we study the electronic states at $n = 2.0$, which is close to the VHS filling ($n_{\text{VHS}} = 2.07$). Figure 1(c) shows the Fermi surfaces (FSs) of the TBG for $\xi = \pm 1$. The weights of two same-valley orbitals on each FS are almost the same. For each valley, there are three VHS points at $E_{\text{VHS}} \sim 0.5$ meV, which locate near the FS for the valley ξ around the M points, as shown in Fig. 1(c). Figures 1(d) and (e) show the band structure with $\xi = \pm 1$ and the total DOS, respectively. The energy structure of the DOS is consistent with the STM measurement [19].

We calculate the spin (charge) susceptibilities $\chi^{s(c)}(\mathbf{q})$ for $\mathbf{q} = (\mathbf{q}, \omega_m = 2m\pi T)$ based on the random-phase-approximation (RPA). Details of formulation are presented in SM A [51]. $\chi^{s(c)}(\mathbf{q}) \propto (1 - \alpha_{s(c)})^{-1}$ is given by the spin (charge) Stoner factor $\alpha_{s(c)}$ [51]. $\alpha_{s(c)} = 1$ corresponds to spin (charge)-ordered state. In the present study, $\alpha_s = \alpha_c = \alpha$ is satisfied due to the relations $U' = U$ and $J = 0$ [38]. Hereafter, we fix $T = 1.5$

meV and the Stoner factor $\alpha = 0.83$ by adjusting the solo model parameter U . $\alpha = 0.83$ corresponds to the moderately correlated region.

Figure 2(a) shows the obtained spin susceptibility $\chi_{1,1;1,1}^s(\mathbf{q}, 0)$, which shows broad maximum peak at the intra-orbital nesting \mathbf{Q} around the VHS. We stress that the valley susceptibility $\chi_{\text{valley}}^c \equiv \chi_{1,1;1,1}^c - \chi_{1,1;3,3}^c$ is exactly the same as $\chi_{1,1;1,1}^s$ in the RPA due to $U' = U$ and $J = 0$ in the TBG. This result is explained by the mean field energy for the valley channel $-\frac{2U'-U}{8}\langle n_{1\uparrow} + n_{1\downarrow} - n_{3\uparrow} - n_{3\downarrow} \rangle$ and that for the spin channel $-\frac{U}{8}\langle n_{1\uparrow} - n_{1\downarrow} + n_{3\uparrow} - n_{3\downarrow} \rangle$, both of which have the same interaction $-\frac{U}{8}$. Here, $n_{l\sigma}$ denotes number of electrons for the orbital l and spin σ . The absence of the Hund's coupling in the TBG is significantly different from usual transition metal compounds ($J/U \gtrsim 0.1$).

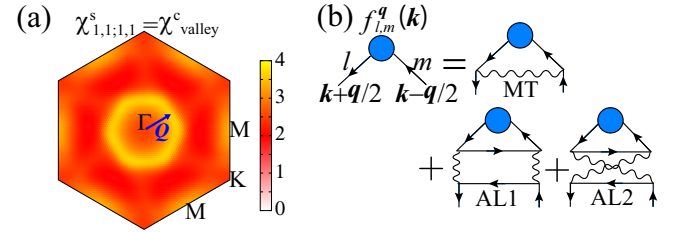


FIG. 2. (a) \mathbf{q} dependences of $\chi_{1,1;1,1}^s(\mathbf{q}, 0) = \chi_{\text{valley}}^c(\mathbf{q}, 0)$ given by the RPA for $n = 2.0$. (b) Feynman diagrams of the DW equation. Each wavy line represents valley+spin fluctuation-mediated interaction.

Hereafter, we derive the most strongest charge-channel density-wave (DW) instability, without assuming the order parameter and the wave vector. For this purpose, we use the DW equation method developed in Refs. [40, 42, 52]. We can derive the optimized non-local form factor $\hat{f}^{\mathbf{q}}$ with the momentum and orbital dependences by solving the following linearized DW equation:

$$\lambda_{\mathbf{q}} f_{l,l'}^{\mathbf{q}}(k) = \frac{T}{N} \sum_{k', m, m'} K_{l,l'; m, m'}^{\mathbf{q}}(k, k') f_{m, m'}^{\mathbf{q}}(k'), \quad (2)$$

where $\lambda_{\mathbf{q}}$ is the eigenvalue of the form factor $\hat{f}^{\mathbf{q}}$. The charge-channel DW with wavevector \mathbf{q} is established when the largest $\lambda_{\mathbf{q}} = 1$. The DW susceptibility is proportional to $(1 - \lambda_{\mathbf{q}})^{-1}$. Therefore, $\lambda_{\mathbf{q}}$ represents the strength of the DW instability. Details of the kernel function $\hat{K}^{\mathbf{q}}(k, k')$ are given in SM A [51]. The Maki-Thompson (MT) terms and Aslamazov-Larkin (AL) terms shown in Fig. 2(b) are included in the kernel function. In the presence of valley and spin fluctuations at $\mathbf{q} = \mathbf{Q}$ and \mathbf{Q}' , the AL terms are strongly enhanced in proportion to $\sum_p \chi(p) \chi(-p + \mathbf{q}_c)$, where $\chi(\mathbf{q})$ is the valley or spin susceptibility. As a result, quantum interference mechanism causes the charge-channel DW order at $\mathbf{q}_c \approx \mathbf{Q} + \mathbf{Q}'$ as shown in Fig. 1(a).

Figure 3(a) shows the \mathbf{q} dependence of the obtained $\lambda_{\mathbf{q}}$. Apparently, ferro ($\mathbf{q} = \mathbf{0}$) DW order is obtained

in the present study. Figure 3(b) shows the dominant static form factor $f_{1,1}^0(\mathbf{k})$, which is derived from the analytic continuation of $\hat{f}^q(\mathbf{k})$. The obtained form factor has no inter-valley component, and satisfies the time reversal invariance. Apparently, the C_3 symmetry is violated by this form factor. The obtained $\hat{f}^0(\mathbf{k})$ belongs to the two-dimensional E representation in the group theory, and its partner $\hat{f}'^0(\mathbf{k})$ is shown in SM B [51]. Thus, the direction of anisotropy can be rotated by making the linear combination of $\hat{f}^0(\mathbf{k})$ and $\hat{f}'^0(\mathbf{k})$.

The obtained nematic state is mainly even parity, as recognized in Fig. 3(b). However, sizable odd-parity component is accompanied since the TBG has no inversion symmetry. To show this, we perform the Fourier transformation of the obtained nematic form factors $\tilde{f}_{l,m}(\mathbf{r}) = \frac{1}{N} \sum_{\mathbf{k}} f_{l,m}^0(\mathbf{k}) e^{i\mathbf{k} \cdot \mathbf{r}}$. Figure 3(c) shows its real part $\text{Re}\tilde{f}_{1,1}(\mathbf{r})$, which gives the bond order (= modulation of the hopping integrals) between the position $\mathbf{0}$ and \mathbf{r} . On the other hand, its imaginary part $\text{Im}\tilde{f}_{1,1}(\mathbf{r})$ in Fig. 3(d) has odd parity, which gives the charge current (see Fig. 4(d)). However, the charge current in one valley is canceled by that in the opposite valley.

The $\mathbf{q} = \mathbf{0}$ nematic order originates from the AL type quantum interference between the valley+spin fluctuations with $\mathbf{Q} \approx -\mathbf{Q}'$ shown in Fig. 1(a). Both valley and spin fluctuations contribute to the nematicity in the TBG. In contrast, only spin fluctuations contribute to the nematic order in Fe-based superconductors with $J \gtrsim 0.1$ [39–46] and cuprate superconductors with single orbital [47]. For this reason, the nematic order is more easily realized in the TBG.

One of the main merit of the present bond-order theory is that the ferro ($\mathbf{q} = \mathbf{0}$) order is naturally obtained. Moreover, the present bond-order theory can cooperate with the phonon mechanism proposed in Ref. [23], according to the discussion in Ref. [53], while the phonon mechanism alone may give the bond order at $\mathbf{q} \approx \mathbf{Q}$. The nematic state was also discussed from the side of electron correlation by using the RG theory [24], by which the AL-type vertex correction (VC) are calculated [45, 46]. Therefore, the difference between the results of the present theory and those in Ref. [24] may originate from the difference of the theoretical models.

Here, we discuss the robustness of the $\mathbf{q} = \mathbf{0}$ nematic bond order. In the present TBG model, the $\mathbf{q} = \mathbf{0}$ nematic bond order is obtained for $-0.3 \lesssim n - n_{\text{VHS}} \lesssim 0$. In SM C [51], we also analyze the form factors based on the original first-principles model with $n_{\text{VHS}} = 0.7$ [49]. It is verified that the $\mathbf{q} = \mathbf{0}$ nematic bond order is also obtained slightly below the VHS filling in the original first-principles model. Thus, the $\mathbf{q} = \mathbf{0}$ nematic bond order is robust for $n \sim n_{\text{VHS}}$ in the TBG.

In the following, we explain the electronic states under the nematic order. We denote Δf as the maximum value of $|\hat{f}^0(\mathbf{k})|$. Figure 4 (a) shows the FSs under the nematic

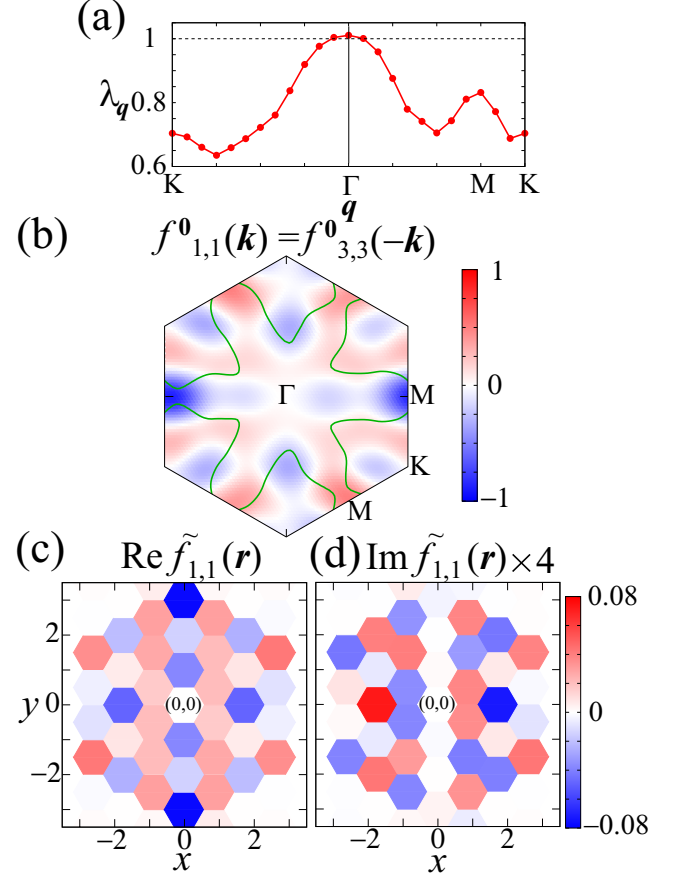


FIG. 3. (a) Obtained \mathbf{q} dependence of λ_q for $n = 2.0$. Its maximum peak at $\mathbf{q} = \mathbf{0}$ means the emergence of the ferro nematic order. (b) Dominant form factor $f_{1,1}^0(\mathbf{k})$ in the Brillouin zone. The green lines indicate FSs for $\xi = +1$. The intra- (inter-) valley relation $f_{1,1}^0(\mathbf{k}) = f_{2,2}^0(\mathbf{k})$ ($f_{1,1}^0(\mathbf{k}) = f_{3,3}^0(-\mathbf{k})$) is satisfied. (c) $\text{Re}\tilde{f}_{1,1}(\mathbf{r})$, which gives the bond order between the position $\mathbf{0}$ and \mathbf{r} . The BA spot (orbitals 1 and 3) locates on the center of hexagon. (d) $\text{Im}\tilde{f}_{1,1}(\mathbf{r})$, which gives the current order.

order. We confirm that the C_3 symmetry is broken by the nematic order, and strong anisotropy appears along the x axis, which is consistent with experiments [19–22]. The band structure for $\Delta f = 5$ meV is shown in Fig. 4 (b). The decrease of energy for $\xi = \pm 1$ at the M ($\pi, 0$) point is explained by the \mathbf{k} dependence of $f_{1,1}^0(\mathbf{k})$ in Fig. 3 (b). Figure 4 (c) shows the DOS under the nematic order $\Delta f = 5$ meV. The energy of the VHS splits into $E_{\text{VHS}} \sim \pm \Delta f$, since the energies of the VHS near $\mathbf{k} = (\pi, 0)$ decrease, and those of other VHS increase due to the \mathbf{k} dependence of $\hat{f}^0(\mathbf{k})$. Thus, the dip structure in the DOS appears near the Fermi energy $E = 0$, which is consistent with STM measurement [19].

Finally, we discuss the time-reversal-symmetry-broken order obtained by the present theory at $n = 2.4$. Figures 5(a) and (b) show the FSs and obtained form factor $\text{Re}f_{1,1}^{Q_1}(\mathbf{k})$ for $\mathbf{Q}_1 \sim 2\mathbf{Q}$, respectively. The ob-

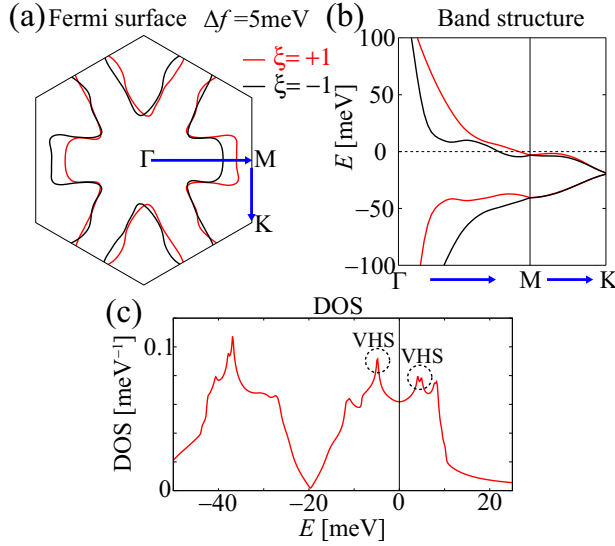


FIG. 4. (a) FSs and (b) band structure under the nematic order with $\Delta f = 5$ meV, where red (black) lines denote $\xi = +1$ (-1). Blue arrows represent the \mathbf{k} path. (c) DOS for $\Delta f = 5$ meV, where the dotted circles show the VHS peak at $E_{\text{VHS}} \sim \pm \Delta f$.

tained $\hat{f}^{\mathbf{Q}_1}(\mathbf{k})$ violates time-reversal-symmetry relation $f_{1,1}^{\mathbf{Q}_1}(\mathbf{k}) = f_{3,3}^{-\mathbf{Q}_1*}(-\mathbf{k})$. This order brings the time-reversal-symmetry-broken valley polarization. This valley polarized state is caused by the cooperation among the inter-valley Hartree term and the AL type quantum interference with $\mathbf{Q} = \mathbf{Q}'$ in Fig. 1(a). \mathbf{q} dependence of $\lambda_{\mathbf{q}}$ is shown in SM D [51]. The relations $U' = U$ and $J = 0$ are important to realized the valley polarization in the TBG.

We stress that interesting charge loop current emerges in the valley polarized phase. Figure 5(c) shows current $j_{1,1}(\mathbf{r})$ for the orbital 1 from the position $\mathbf{0}$ to \mathbf{r} for $U = U' = 0$ in the unit of $1 \text{ meV}/\hbar$: $j_{1,1}(\mathbf{r}) = -2\text{Im}\langle \tilde{h}_{1,1}^0(\mathbf{r})c_1^\dagger(\mathbf{r})c_1(\mathbf{0}) \rangle$, where $\tilde{h}_{1,1}^0(\mathbf{r})$ is the hopping integral of the tight-binding model. Thus, the C_3 symmetry loop current appears in each valley due to the imaginary hopping integrals in \tilde{h}^0 . Figure 5 (d) shows the intra-orbital current pattern between the nearest sites, in the case of $\mathbf{q} = \mathbf{0}$ for simplicity. Since the direction of rotation in loop current $j_{1,1}$ between the BA sites is opposite to that in $j_{2,2}$ between the AB sites, the effective magnetic flux is opposite to the adjacent ones as shown in Fig. 5(d). Because of the relation $j_{1,1}(\mathbf{r}) = -j_{3,3}(\mathbf{r})$, the C_3 symmetry loop current is canceled between the opposite valleys, and it is identified as the valley loop current. In the presence of the valley polarization, the energy shift $\Delta E^\xi \sim \xi \text{Re}f_{1,1}^{\mathbf{Q}_1}$ for the valley $\xi = \pm 1$ appears. Since the ΔE^ξ makes unbalance between the currents for $\xi = \pm 1$, the valley loop current is converted to the net charge loop current, which has been frequently discussed in cuprates [54, 55]. The magnetic flux emerges

in proportion to $|\Delta E^\xi|$, and it is measurable by several experimental methods. We note that the obtained $\mathbf{q} \neq \mathbf{0}$ valley polarization induces a staggered charge loop current.

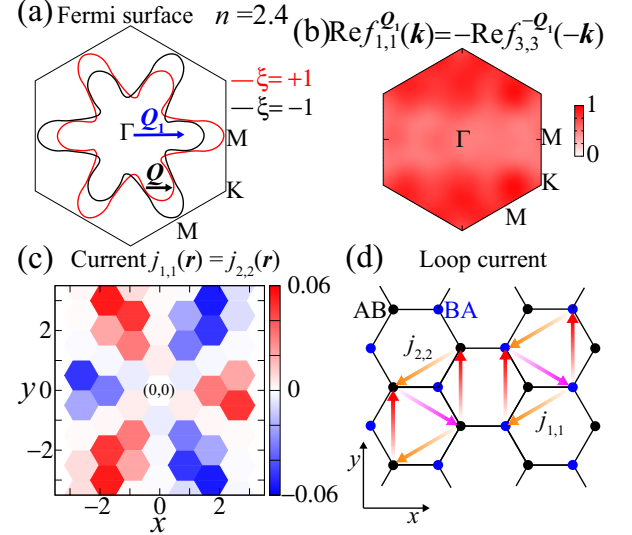


FIG. 5. (a) FSs for $n = 2.4$. (b) Obtained form factor $f_{1,1}^{\mathbf{Q}_1}(\mathbf{k})$, which breaks the time reversal symmetry. The intra- (inter-) valley relation $\text{Re}f_{1,1}^{\mathbf{Q}_1}(\mathbf{k}) = \text{Re}f_{2,2}^{\mathbf{Q}_1}(\mathbf{k})$ ($\text{Re}f_{1,1}^{\mathbf{Q}_1}(\mathbf{k}) = -\text{Re}f_{3,3}^{-\mathbf{Q}_1}(-\mathbf{k})$) is satisfied. (c) C_3 symmetry current $j_{1,1}(\mathbf{r}) [= j_{2,2}(\mathbf{r})]$ without the form factor, where the BA spot (orbitals 1 and 3) locates on the center of hexagon. (d) Schematic picture of the loop current $j_{1,1}(\mathbf{r})$ and $j_{2,2}(\mathbf{r})$ between the nearest intra-orbital sites. In the valley polarized state, this valley loop current changes to the charge loop current.

In summary, we studied the origin of the nematic state in the TBG. We found that the $\mathbf{q} = \mathbf{0}$ C_3 -symmetry-breaking nematic state near the VHS filling is identified as the nematic bond order. This order is driven by the quantum interference among the valley + spin fluctuations thanks to the Hund's less nature of the TBG. This mechanism of nematicity is insensitive to the model parameters as verified in SM C [51]. We also found the emergence of the time-reversal-symmetry-broken valley polarization, which accompanies the novel charge loop current near the nematic phase. The present study revealed unexpected interesting similarities and differences between the TBG and Fe-based superconductors.

We are grateful to Y. Yamakawa for useful discussions. This work was supported by Grants-in-Aid for Scientific Research from MEXT, Japan (No. JP19H05825, No. JP18H01175, and No. JP17K05543).

[1] Y. Cao, V. Fatemi, S. Fang, K. Watanabe, T. Taniguchi, E. Kaxiras, and P. Jarillo-Herrero, *Nature* **556**, 43 (2018).

- [2] Y. Cao, V. Fatemi, A. Demir, S. Fang, S. L. Tomarken, J. Y. Luo, J. D. Sanchez-Yamagishi, K. Watanabe, T. Taniguchi, E. Kaxiras, R. C. Ashoori, and P. Jarillo-Herrero, *Nature* **556**, 80 (2018).
- [3] M. Yankowitz, S. Chen, H. Polshyn, Y. Zhang, K. Watanabe, T. Taniguchi, D. Graf, A. F. Young, and C. R. Dean, *Science* **363**, 1059 (2019).
- [4] X. Lu, P. Stepanov, W. Yang, M. Xie, M. A. Aamir, I. Das, C. Urgell, K. Watanabe, T. Taniguchi, G. Zhang, A. Bachtold, A. H. MacDonald, and D. K. Efetov, *Nature* **574**, 653 (2019).
- [5] C. Xu and L. Balents, *Phys. Rev. Lett.* **121**, 087001 (2018).
- [6] J. F. Dodaro, S. A. Kivelson, Y. Schattner, X. Q. Sun, and C. Wang, *Phys. Rev. B* **98**, 075154 (2018).
- [7] J. W. F. Venderbos and R. M. Fernandes, *Phys. Rev. B* **98**, 245103 (2018).
- [8] H. Isobe, N. F. Q. Yuan, and L. Fu, *Phys. Rev. X* **8**, 041041 (2018).
- [9] J. Kang and O. Vafek, *Phys. Rev. Lett.* **122**, 246401 (2019).
- [10] Y.-P. Lin and R. M. Nandkishore, *Phys. Rev. B* **100**, 085136 (2019).
- [11] B. Roy and V. Juricic, *Phys. Rev. B* **99**, 121407(R) (2019).
- [12] S. Ray, J. Jung, and T. Das, *Phys. Rev. B* **99**, 134515 (2019).
- [13] Y.-Z. You and A. Vishvanath, *npj Quantum Mater.* **4**, 16 (2019).
- [14] Y.-H. Zhang, D. Mao, and T. Senthil, *Phys. Rev. Research* **1**, 033126 (2019).
- [15] D. V. Chichinadze, L. Classen, and A. V. Chubukov, *Phys. Rev. B* **101**, 224513 (2020).
- [16] Y. Wang, J. Kang, and R. M. Fernandes, *arXiv:2009.01237* (2020).
- [17] M. Xie and A. H. MacDonald, *Phys. Rev. Lett.* **124**, 097601 (2020).
- [18] N. Bultinck, S. Chatterjee and M. P. Zaletel, *Phys. Rev. Lett.* **124**, 166601 (2020).
- [19] A. Kerelsky, L. McGilly, D. M. Kennes, L. Xian, M. Yankowitz, S. Chen, K. Watanabe, T. Taniguchi, J. Hone, C. Dean, A. Rubio, and A. N. Pasupathy, *Nature* **572**, 95 (2019).
- [20] Y. Choi, J. Kemmer, Y. Peng, A. Thomson, H. Arora, R. Polski, Y. Zhang, H. Ren, J. Alicea, G. Refael, F. von Oppen, K. Watanabe, T. Taniguchi, and S. Nadj-Perge, *Nat. Phys.* **15**, 1174 (2019).
- [21] Y. Jiang, X. Lai, K. Watanabe, T. Taniguchi, K. Haule, J. Mao, and E. Y. Andrei, *Nature* **573**, 91 (2019).
- [22] Y. Cao, D. R. Legrain, J. M. Park, F. N. Yuan, K. Watanabe, T. Taniguchi, R. M. Fernandes, L. Fu, P. J. Herrero, *arXiv:2004.04148* (2020).
- [23] R. M. Fernandes and J. W. F. Venderbos, *Sci. Adv.* **6**, eaba8834 (2020).
- [24] D. V. Chichinadze, L. Classen, and A. V. Chubukov, *arXiv:2007.00871* (2020).
- [25] D. C. Johnston, *Adv. Phys.* **59**, 803 (2010).
- [26] Y. Mizuguchi and Y. Takano, *J. Phys. Soc. Jpn.* **79**, 102001 (2010).
- [27] Y. Sato, S. Kasahara, H. Murayama, Y. Kasahara, E.-G. Moon, T. Nishizaki, T. Loew, J. Porras, B. Keimer, T. Shibauchi, and Y. Matsuda, *Nat. Phys.* **13**, 1074 (2017).
- [28] R. M. Fernandes, L. H. VanBebber, S. Bhattacharya, P. Chandra, V. Keppens, D. Mandrus, M. A. McGuire, B. C. Sales, A. S. Sefat, and J. Schmalian, *Phys. Rev. Lett.* **105**, 157003 (2010).
- [29] R. M. Fernandes, E. Abrahams, and J. Schmalian, *Phys. Rev. Lett.* **107**, 217002 (2011).
- [30] F. Wang, S. A. Kivelson, and D.-H. Lee, *Nat. Phys.* **11**, 959 (2015).
- [31] R. Yu, and Q. Si, *Phys. Rev. Lett.* **115**, 116401 (2015).
- [32] J. K. Glasbrenner, I. I. Mazin, H. O. Jeschke, P. J. Hirschfeld, and R. Valenti, *Nat. Phys.* **11**, 953 (2015).
- [33] C. Fang, H. Yao, W.-F. Tsai, J. P. Hu, and S. A. Kivelson, *Phys. Rev. B* **77**, 224509 (2008).
- [34] R. M. Fernandes and A. V. Chubukov, *Rep. Prog. Phys.* **80**, 014503 (2017).
- [35] F. Krüger, S. Kumar, J. Zaanen, J. van den Brink, *Phys. Rev. B* **79**, 054504 (2009).
- [36] W. Lv, J. Wu, and P. Phillips, *Phys. Rev. B* **80**, 224506 (2009).
- [37] C.-C. Lee, W.-G. Yin, and W. Ku, *Phys. Rev. Lett.* **103**, 267001 (2009).
- [38] H. Kontani and S. Onari, *Phys. Rev. Lett.* **104**, 157001 (2010).
- [39] S. Onari and H. Kontani, *Phys. Rev. Lett.* **109**, 137001 (2012).
- [40] S. Onari, Y. Yamakawa, and H. Kontani, *Phys. Rev. Lett.* **116**, 227001 (2016).
- [41] Y. Yamakawa, S. Onari and H. Kontani, *Phys. Rev. X* **6**, 021032 (2016).
- [42] S. Onari and H. Kontani, *Phys. Rev. B* **100**, 020507(R) (2019).
- [43] K. Jiang, J. Hu, H. Ding, and Z. Wang, *Phys. Rev. B* **93**, 115138 (2016).
- [44] L. Fanfarillo, G. Giovannetti, M. Capone, and E. Bascones, *Phys. Rev. B* **95**, 144511 (2017).
- [45] R. Q. Xing, L. Classen, A. V. Chubukov, *Phys. Rev. B* **98**, 041108(R) (2018).
- [46] A. V. Chubukov, M. Khodas, and R. M. Fernandes, *Phys. Rev. X* **6**, 041045 (2016).
- [47] M. Tsuchiizu, K. Kawaguchi, Y. Yamakawa, and H. Kontani, *Phys. Rev. B* **97**, 165131 (2018).
- [48] M. Tsuchiizu, Y. Ohno, S. Onari, and H. Kontani, *Phys. Rev. Lett.* **111**, 057003 (2013).
- [49] M. Koshino, N. F. Q. Yuan, T. Koretsune, M. Ochi, K. Kuroki, and L. Fu, *Phys. Rev. X* **8**, 031087 (2018).
- [50] M. J. Klug, *New J. Phys.* **22**, 073016 (2020).
- [51] Supplemental Material
- [52] H. Kontani, Y. Yamakawa, R. Tazai, and S. Onari, *arXiv:2003.07556* (2020).
- [53] H. Kontani, T. Saito, and S. Onari, *Phys. Rev. B* **84**, 024528 (2011).
- [54] I. Affleck and J. B. Marston, *Phys. Rev. B* **37**, 3774(R) (1988).
- [55] C. M. Varma, *Phys. Rev. B* **55**, 14554 (1997).

[Supplementary Material]

Nematic Order in Twisted Bilayer Graphene by Valley + Spin Fluctuation Interference Mechanism

Seiichiro Onari and Hiroshi Kontani

Department of Physics, Nagoya University, Nagoya 464-8602, Japan

A: Model Hamiltonian of the TBG, formalism of the RPA and the DW equation

First, we introduce model for the TBG by referring the first-principles tight-binding model in Ref. [1]. However, in this original model, the VHS appears near $n \sim 0.7$, which is different from the experimentally observed $n_{\text{VHS}} \sim 2$ [2]. Figure S1(a) shows the band structure of the original model for $n = 0.5$, where all the hopping integrals are magnified 50 times in order to fit the bandwidth observed by the STM measurement [2]. To shift the VHS filling to the experimental one, we reduce the magnitude of the imaginary part of second-nearest intra-orbital hopping 0.097 meV to 0.03 meV, while the real part is fixed. Also, we reduce the magnitude of the imaginary part of fourth-nearest intra-orbital hopping 0.039 meV to 0.02 meV. Finally, we magnify all the hopping integrals 50 times. Figures S1(b), (c), and (d) show the band structure, the DOS, and $\chi_{1,1;1,1}^c(\mathbf{q}, 0)$ in the obtained model, respectively. At $n = 2.4$, the Fermi energy ($E = 0$) is above the energy of VHS. Although the band structure in the present model is similar to that the original model, the energy difference between the valleys near the Fermi energy along Γ -M line increases in the present model.

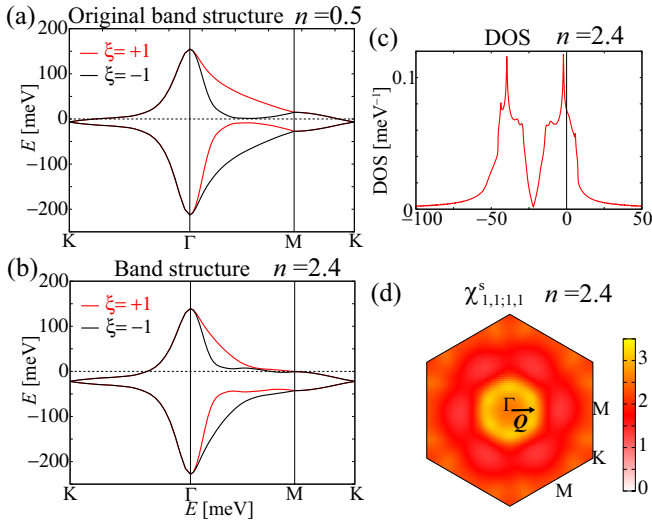


FIG. S1. (a) Band structure in the original model for $n = 0.5$, where red (black) lines denote valley $\xi = +1$ (-1). (b) Band structure in the present model for $n = 2.4$. (c) DOS and (d) $\chi_{1,1;1,1}^c(\mathbf{q}, 0)$ for $n = 2.4$. Arrow \mathbf{Q} denotes the nesting vector.

Here, we explain the Coulomb interaction introduced

in the present study. Only the Coulomb interactions between the orbitals with the same center position are taken into account. The Coulomb interaction for the spin channel in the main text is

$$(\Gamma^s)_{l_1 l_2, l_3 l_4} = \begin{cases} U, & l_1 = l_2 = l_3 = l_4 \\ U', & l_1 = l_3 = l_2 \pm 2 = l_4 \pm 2 \\ J, & l_1 = l_2 = l_3 \pm 2 = l_4 \pm 2 \\ J, & l_1 = l_4 = l_2 \pm 2 = l_3 \pm 2 \\ 0, & \text{otherwise.} \end{cases} \quad (\text{S1})$$

Furthermore, the Coulomb interaction for the charge channel is

$$(\hat{\Gamma}^c)_{l_1 l_2, l_3 l_4} = \begin{cases} -U, & l_1 = l_2 = l_3 = l_4 \\ U' - 2J, & l_1 = l_3 = l_2 \pm 2 = l_4 \pm 2 \\ -2U' + J, & l_1 = l_2 = l_3 \pm 2 = l_4 \pm 2 \\ -J, & l_1 = l_4 = l_2 \pm 2 = l_3 \pm 2 \\ 0, & \text{otherwise.} \end{cases} \quad (\text{S2})$$

We set $U' = U$ and $J = 0$ in the present study according to Ref. [1]. Here, we drop the inter-site Coulomb interaction $V_{\mathbf{r}, \mathbf{r}'}$, because of the following reasons; In the RPA, the spin fluctuations and valley fluctuations are not affected by $V_{\mathbf{r}, \mathbf{r}'}$. Moreover, $\lambda_{\mathbf{q}}$ for the nearest neighbor $V_{\mathbf{r}, \mathbf{r}'} < \frac{U}{2}$ ($\alpha_c < 0.95$) is almost the same as that without $V_{\mathbf{r}, \mathbf{r}'}$. Therefore, we neglect $V_{\mathbf{r}, \mathbf{r}'}$ in the main text, by expecting the screening effect on $V_{\mathbf{r}, \mathbf{r}'}$.

By using the multiorbital Coulomb interaction, the spin (charge) susceptibility in the RPA is given by

$$\hat{\chi}^{s(c)}(\mathbf{q}) = \hat{\chi}^0(\mathbf{q})[1 - \hat{\Gamma}^{s(c)}\hat{\chi}^0(\mathbf{q})]^{-1}, \quad (\text{S3})$$

where the irreducible susceptibility is

$$\chi_{l, l'; m, m'}^0(\mathbf{q}) = -\frac{T}{N} \sum_{\mathbf{k}} G_{l, m}(\mathbf{k} + \mathbf{q}) G_{m', l'}(\mathbf{k}). \quad (\text{S4})$$

$\hat{G}(\mathbf{k})$ is the multiorbital Green function without self-energy $\hat{G}(\mathbf{k}) = [(i\epsilon_n - \mu)\hat{1} - \hat{h}^0(\mathbf{k})]^{-1}$ for $\mathbf{k}, \epsilon_n = (2n+1)\pi T$. Here, $\hat{h}^0(\mathbf{k})$ is the matrix expression of H^0 and μ is the chemical potential.

The spin (charge) Stoner factor $\alpha_{s(c)}$ is defined as the maximum eigenvalue of $\hat{\Gamma}^{s(c)}\hat{\chi}^0(\mathbf{q}, 0)$. $\alpha_c = \alpha_s = \alpha$ is satisfied due to the relations $J = 0$ and $U' = U$. In the present study, we fix $\alpha = 0.83$ and $T = 1.5$ meV, b setting $U = 39$ (42) meV for $n = 2.0$ (2.4). (U is the solo

parameter in the present study.) We use $N = 72 \times 72$ \mathbf{k} meshes and 512 Matsubara frequencies.

The kernel function $\hat{K}^q(k, k')$ in the DW equation [3, 4] is given by

$$K_{l,l';m,m'}^q(k, k') = - \sum_{m_1, m_2} I_{l,l';m_1, m_2}^q(k, k') g_{m_1, m_2; m, m'}^q(k'), \quad (\text{S5})$$

where $g_{l,l';m,m'}^q(k) \equiv G_{l,m}(k + \frac{\mathbf{q}}{2}) G_{m',l'}(k - \frac{\mathbf{q}}{2})$, and $\hat{I}^q(k, k')$ is the four-point vertex.

$\hat{I}^q(k, k')$ is given as

$$\begin{aligned} I_{l,l';m,m'}^q(k, k') = & \sum_{b=s,c} \left[-\frac{a^b}{2} V_{l,m;l',m'}^b(k - k') \right. \\ & + \frac{T}{N} \sum_{p,l_1,l_2,m_1,m_2} \frac{a^b}{2} V_{l,l_1;l_2,m_2}^b \left(p + \frac{\mathbf{q}}{2} \right) V_{m',l_2;l',m_1}^b \left(p - \frac{\mathbf{q}}{2} \right) \\ & \quad \times G_{l_1,m_1}(k - p) G_{l_2,m_2}(k' - p) \\ & + \frac{T}{N} \sum_{p,l_1,l_2,m_1,m_2} \frac{a^b}{2} V_{l,l_1;l_2,m_1}^b \left(p + \frac{\mathbf{q}}{2} \right) V_{m_2,m;l',m_1}^b \left(p - \frac{\mathbf{q}}{2} \right) \\ & \quad \times G_{l_1,m_1}(k - p) G_{l_2,m_2}(k' + p) \Big], \quad (\text{S6}) \end{aligned}$$

where $a^s = 3$, $a^c = 1$, $p = (\mathbf{p}, \omega_l)$, and $\hat{V}^{s(c)}(q) = \hat{\Gamma}^{s(c)} + \hat{\Gamma}^{s(c)} \hat{\chi}^{s(c)}(q) \hat{\Gamma}^{s(c)}$.

In Eq. (S6), the first line corresponds to the Maki-Thompson (MT) term, and the second and third lines give the AL1 and AL2 terms, respectively. In the MT term, the first-order term with respect to $\hat{\Gamma}^{s,c}$ gives the Hartree-Fock (HF) term in the mean-field theory.

B: Detailed results of the form factor for $n = 2.0$

Here, we explain details of obtained $\mathbf{q} = \mathbf{0}$ form factor in TBG. In the main text, we show only the diagonal form factor in Fig. 3 (b). Figure S2(a) show the off-diagonal form factor $f_{1,2}^0(\mathbf{k})$, which is a little smaller than the diagonal form factor. The Fourier transformed form factor $\tilde{f}_{1,2}(\mathbf{r})$ is shown in Fig. S2(b). These form factors are invariant under the time reversal operation [$f_{1,2}^0(\mathbf{k}) = f_{3,4}^{0*}(-\mathbf{k})$, $\tilde{f}_{1,2}(\mathbf{r}) = \tilde{f}_{3,4}^*(\mathbf{r})$]. The real part $\text{Re} \tilde{f}_{1,2}(\mathbf{r}) = \text{Re} \tilde{f}_{2,1}(-\mathbf{r})$ corresponds to the bond order, and the imaginary part $\text{Im} \tilde{f}_{1,2}(\mathbf{r}) = -\text{Im} \tilde{f}_{2,1}(-\mathbf{r})$ is the origin of valley current. The obtained form factors belong to the two-dimensional E representation in the group theory, and the other form factors \hat{f}^0 with the same λ_0 is shown in Figs. S3(a) and (b). The direction of anisotropy is different from that in the main text. Thus, we can rotate the direction of anisotropy by making the linear combination of \hat{f}^0 and $\hat{f}^{0'}$.

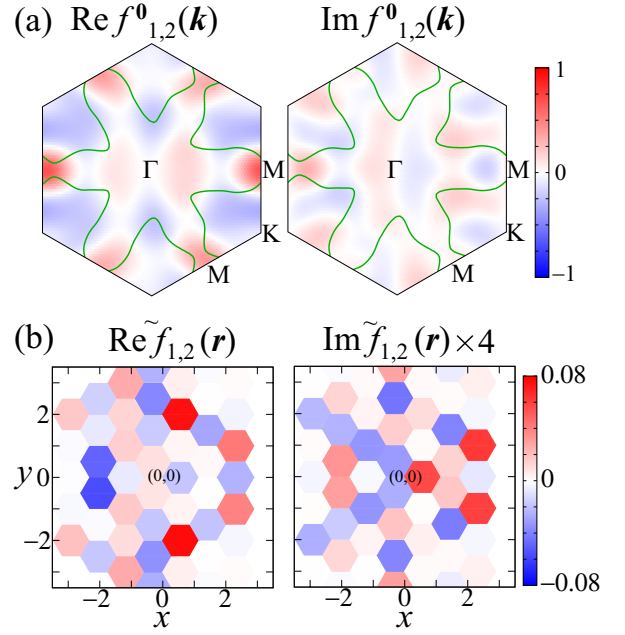


FIG. S2. (a) Off-diagonal form factor explained in the main text for $n = 2.0$, and (b) $\text{Re} \tilde{f}_{1,2}(\mathbf{r})$ and $\text{Im} \tilde{f}_{1,2}(\mathbf{r})$ of the form factor. The green lines indicate FSs for $\xi = +1$. Centers of orbital 1 and 2 locate on the center and corner of hexagon, respectively.

C: Nematic state obtained by the original Koshino model

In the present study, we introduced minimum additional terms into the original Koshino model [1] in order to realize the experimental VHS filling $n_{\text{VHS}} \sim 2$ [2]. Based on the modified model explained in SM A, we explain the emergence of the nematic bond order in the TBG in the main text. The obtained nematic bond order is consistent with experimental results [2]. We clarify that the origin of the nematicity is the valley+spin fluctuation interference due to the AL-type VC.

Here, in order to verify the validity of the present mechanism of the nematic bond order, we investigate the original Koshino model, by multiplying all the hopping integrals by 50 in order to fit the bandwidth obtained by the STM measurement [2]. The FSs and band structure are shown in Figs. S4(a) and S1(a). We stress that the band structure is similar to Fig. 1(d) in the main text. In contrast, the FS structure is very different from Fig. 1(c) in the main text, and the VHS filling $n_{\text{VHS}} = 0.7$ is also very different from $n_{\text{VHS}} = 2.07$ in the main text. Moreover, the positions of the VHS points are different. These differences mainly come from the reduction of the imaginary intra-orbital hoppings.

Nonetheless of the large difference between two models, the nematic state is also obtained in the original Koshino model when the filling is slightly lower than n_{VHS} . Figure

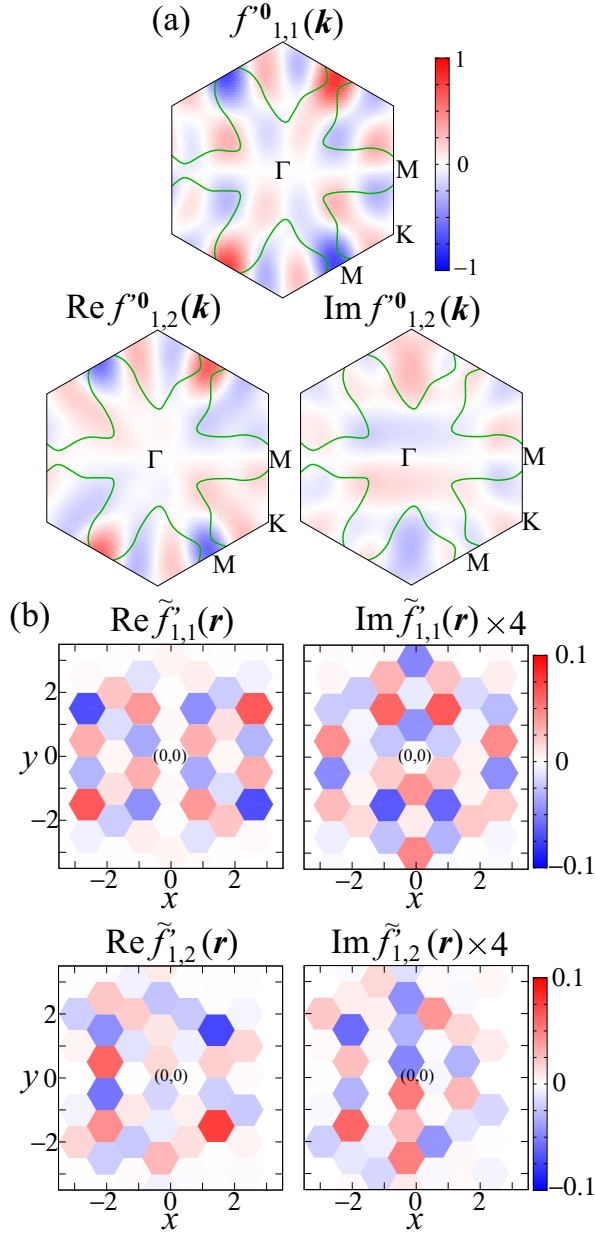


FIG. S3. (a) $f'^0(\mathbf{k})$ and (b) $\tilde{f}'(\mathbf{r})$ of the degenerate form factor for $n = 2.0$. The green lines indicate FSs for $\xi = +1$. Centers of orbital 1 and 2 locate on the center and corner of hexagon, respectively.

S4(b) shows \mathbf{q} dependence of the DW equation eigenvalue $\lambda_{\mathbf{q}}$ for $n = 0.5$ and $\alpha = 0.91$ ($U = 28.7$ meV)

at $T = 1.5$ meV. The obtained $\lambda_{\mathbf{q}}$ has peak at $\mathbf{q} = \mathbf{0}$, which corresponds to the emergence of the $\mathbf{q} = \mathbf{0}$ nematic order. The obtained form factors in Figs. S4(c), (d), (e) are similar to those in Figs. 3(b), (c), (d) in the main text. The real part $\text{Re} \tilde{f}'_{1,1}(\mathbf{r})$ gives the bond order. The imaginary part $\text{Im} \tilde{f}'_{1,1}(\mathbf{r})$ gives the spontaneous current. Thus, the nematic state near the VHS filling is also identified as the nematic bond order based on the original Koshino model. The present solution also belongs to the two-dimensional E representation. Figure S4(f) shows obtained current $j_{1,1}(\mathbf{r})$ from $\mathbf{0}$ to \mathbf{r} for orbital 1 in the unit of $1\text{meV}/\hbar$. $j_{1,1}(\mathbf{r})$ is given by $j_{1,1}(\mathbf{r}) = -2\text{Im}\langle[\tilde{h}_{1,1}^0(\mathbf{r}) + \tilde{f}_{1,1}(\mathbf{r})]c_1^\dagger(\mathbf{r})c_1(\mathbf{0})\rangle$ for the maximum value of form factor $\Delta f = 5\text{meV}$, where $\tilde{h}_{1,1}^0(\mathbf{r})$ is the kinetic Hamiltonian term. We see that the C_3 symmetric current pattern in Fig. 5(c) is broken by the nematic order, and the strong anisotropy appears along the x axis.

In summary, although the value of n_{VHS} and the FS structure are very different between the original Koshino model and the present model in the main text, both models lead to essentially the same nematic bond order solution. Thus, $\mathbf{q} = \mathbf{0}$ nematic bond order is stably obtained near the VHS filling irrespective of huge difference in the FS structure.

D: \mathbf{q} dependence of $\lambda_{\mathbf{q}}$ for $n = 2.4$

We discuss the \mathbf{q} dependence of $\lambda_{\mathbf{q}}$ for $n = 2.4$. Figure S5 shows $\lambda_{\mathbf{q}}$ obtained by the model in the main text. The $\lambda_{\mathbf{q}}$ has peak at $\mathbf{q} = \mathbf{Q}_1 \sim 2\mathbf{Q}$ due to the quantum interference mechanism in Fig 1(a). We confirm that $\lambda_{\mathbf{Q}_1}$ is enlarged by the Hartree term in the MT terms and the AL type quantum interference between the valley + spin fluctuations with $\mathbf{Q} = \mathbf{Q}'$.

-
- [1] M. Koshino, N. F. Q. Yuan, T. Koretsune, M. Ochi, K. Kuroki, and L. Fu, Phys. Rev. X **8**, 031087 (2018).
 - [2] A. Kerelsky, L. McGilly, D. M. Kennes, L. Xian, M. Yankowitz, S. Chen, K. Watanabe, T. Taniguchi, J. Hone, C. Dean, A. Rubio, and A. N. Pasupathy, Nature **572**, 95 (2019).
 - [3] S. Onari, Y. Yamakawa, and H. Kontani, Phys. Rev. Lett. **116**, 227001 (2016).
 - [4] S. Onari and H. Kontani, Phys. Rev. B **100**, 020507(R) (2019).

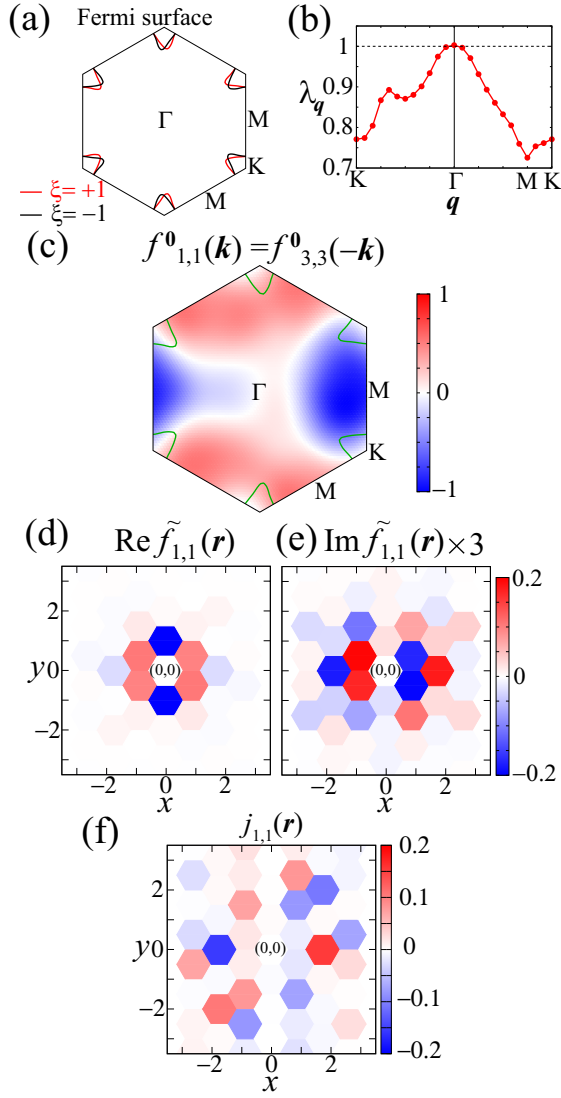


FIG. S4. (a) FSs for $n = 0.5$ in the original model, where red (black) lines denote the valley $\xi = +1$ (-1). (b) Obtained q dependence of λ_q for $n = 0.5$ in the original model. (c) Form factor $f_{1,1}^0(\mathbf{k})$ in the Brillouin zone. The green lines indicate FSs for $\xi = +1$. (d) $\text{Re} \tilde{f}_{1,1}(\mathbf{r})$ and (e) $\text{Im} \tilde{f}_{1,1}(\mathbf{r})$, which gives the bond-order and current order, respectively. The BA spot (orbitals 1 and 3) locates on the center of hexagon. (f) Current $j_{1,1}(\mathbf{r})$ by the form factor $\tilde{f}_{1,1}(\mathbf{r})$ with $\Delta f = 5$ meV.

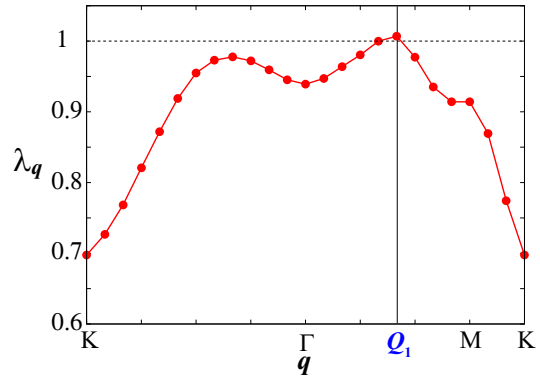


FIG. S5. q dependence of λ_q for $n = 2.4$.